Dependence of skull surface wave propagation on stimulation sites and direction under bone conduction

Dobrev, Ivo ; Farahmandi, Tahmine S ; Sim, Jae Hoon ; Pfiffner, Flurin ; Huber, Alexander M ; Röösli, Christof

DOI: https://doi.org/10.1121/10.0000933

JASA ARTICLE

Dependence of skull surface wave propagation on stimulation sites and direction under bone conduction

Ivo Dobrev,[1,a)] Tahmine S. Farahmandi,[1] Jae Hoon Sim,[2] Flurin Pfiffner,[1] Alexander M. Huber,[2] and Christof Röösli[2]

[1]*Faculty of Science, University of Zürich, Rämistrasse 71, 8006 Zürich, Switzerland*

[2]*Department of Otorhinolaryngology, Head and Neck Surgery, University Hospital Zürich, Rämistrasse 100, 8091 Zürich, Switzerland*

ABSTRACT:

In order to better understand bone conduction sound propagation across the skull, three-dimensional (3D) wave propagation on the skull surface was studied, along with its dependence on stimulation direction and location of a bone conduction hearing aid (BCHA) actuator. Experiments were conducted on five Thiel embalmed whole head cadaver specimens. Stimulation, in the 0.1–10 kHz range, was sequentially applied at the forehead and mastoid via electromagnetic actuators from commercial BCHAs, supported by a 5-N steel band. The head response was quantified by sequentially measuring the 3D motion of ∼200 points (∼15–20 mm pitch) across the ipsilateral, top, and contralateral skull surface via a 3D laser Doppler vibrometer (LDV) system, guided by a robotic positioner. Low-frequency stimulation (<1 kHz) resulted in a spatially complex rigid-body-like motion of the skull that depended on both the stimulation condition and head support. The predominant motion direction was only 5–10 dB higher than other components below 1 kHz, with no predominance at higher frequencies. Sound propagation direction across the parietal plates did not coincide with stimulation location, potentially due to the head base and forehead remaining rigid-like at higher frequencies and acting as a large source for the deformation patterns across the parietal sections.

 https://doi.org/10.1121/10.0000933

(Received 23 September 2019; revised 5 February 2020; accepted 2 March 2020; published online 27 March 2020)

[Editor: G. Christopher Stecker] Pages: 1985–2001

I. INTRODUCTION

Bone conduction hearing aid (BCHA) treatment has become the standard of care for patients suffering from conductive or mixed hearing loss who cannot wear conventional hearing aids (Hulecki and Small, 2011; Pfiffner *et al.*, 2011). In young children, a BCHA is usually worn on a headband that is placed on the forehead or on the mastoid. Another indication is for patients with single-sided deafness. The aim of BCHAs in this instance is to route sound from the deaf side to the hearing side. The efficacy of the sound propagation by BC from the BCHA to the target ear depends on several important aspects.

First, the propagation of the sound energy could involve several possible pathways through which sound reaches and stimulates the cochlea. Most authors agree that these pathways and their interactions depend on frequency and on the state of the middle ear ossicles (Tonndorf, 1966; Stenfelt, 2006; Stenfelt and Goode, 2005a; Stenfelt, 2016). Five possible pathways have been generally accepted, which can be split into two main groups: (1) osseous pathways involving bone vibration resulting in inertial motion of the inner ear fluid (Kim *et al.*, 2011; Stenfelt, 2015) and middle ear ossicles (Homma *et al.*, 2010; Stenfelt, 2006; Stenfelt *et al.*, 2002) or deformations of the otic capsule (Stenfelt, 2015; Tonndorf, 1966; von Békésy, 1960) and external auditory canal (Brummund *et al.*, 2014; Stenfelt *et al.*, 2003). (2) Non-osseous pathways include sound vibrations of the skin covering the skull or by pressure transmission within the contents of the skull, such as brain tissue and cerebrospinal fluid via the internal auditory canal, cochlear aqueduct, and/or vestibular aqueduct to the cochlea (Sohmer and Freeman, 2004; Sohmer *et al.*, 2000; Sim *et al.*, 2016; Röösli *et al.*, 2016). The contribution of each of these pathways, their interaction and frequency dependency, and how they are activated by different BCHAs to induce the final sensation of hearing is still a matter of debate.

Second, the site of stimulation influences perception. In the case of contralateral stimulation in patients with SSD, sound propagates across the head via one of the abovementioned pathways to stimulate the contralateral cochlea. In such a case, the frequency dependence of the resulting transcranial attenuation is critical for the optimal operation of the BCHA or for sufficient masking during clinical measurements of monaural BC thresholds (Hood, 1960; Studebaker, 1964). However, transcranial attenuation varies considerably between individuals ranging from 0 to 15 dB between 0.25 and 4 kHz (Hurley and Berger, 1970; Snyder, 1973; Nolan and Lyon, 1981; Kompis *et al.*, 2011). The transcranial transmission is frequency and stimulation site dependent as well (Stenfelt and Goode, 2005b; Eeg-Olofsson *et al.*, 2011a; Farrell *et al.*, 2017, Mattingly *et al.*, 2019). The role of the different pathways involved in transcranial transmission is not fully understood.

a)Electronic mail: ivo.dobrev@usz.ch

In the case of ipsilateral simulation, such as for patients with bilateral BCHA, large transcranial attenuation is desired as it is beneficial for binaural hearing (Stenfelt, 2012; Håkansson *et al.*, 2010). There is a general consensus that stimulation closer to the cochlea is more efficient for ipsilateral stimulation (Eeg-Olofsson *et al.*, 2011b) and increases transcranial attenuation (Eeg-Olofsson *et al.*, 2011a). However, the specific mechanisms of this localized transmission, which can be within a few centimeters, are still not completely clear. This has been evidenced by previous studies involving stimulation via headband coupling at several locations near the ear canal that have indicated that stimulation superior-anterior to the pinna is more efficient than behind the pinna (mastoid area) even with a similar distance from the cochlea (Dobrev *et al.*, 2016; Ito *et al.*, 2011).

Several methods exist to quantify crucial parameters of sound propagation under bone conduction stimulation including: (1) response of the outer hair cells via otoacoustic emissions (OAE) (Stump *et al.*, 2018; Watanabe *et al.*, 2008); (2) motion of the temporal bones via laser Doppler vibrometry (LDV) or via accelerometers (Stenfelt *et al.*, 2002; Stenfelt, 2006), including 3D measurements of middle ear structures (Dobrev *et al.*, 2016) and promontory motion (Stenfelt and Goode, 2005a; Eeg-Olofsson *et al.*, 2008; Eeg-Olofsson *et al.*, 2013; Dobrev and Sim, 2018; Dobrev *et al.*, 2019); (3) sound pressure in the cochlea via miniature pressure sensors (Chhan *et al.*, 2013; Stieger *et al.*, 2018; Hartl *et al.*, 2016; Borgers *et al.*, 2019; Mattingly *et al.*, 2019); and (4) sound pressure within the cerebral-spinal fluid (CFS) (Dobrev *et al.*, 2019, Sohmer and Freeman, 2004). Most of the vibration measurement methods used previously have been based on single point measurements via LDV, accelerometer, or impedance head. However, the skull surface exhibits a complex spatial-temporal response to stimulation, as evidence by full-field vibration measurements in dry skulls (Ogura *et al.*, 1979; McKnight *et al.*, 2013), cadaver heads (Dobrev *et al.*, 2017; Hoyer and Dörheide, 1983), and living subjects (McLeod *et al.*, 2018). Thus, 3D velocity scanning methods that allow for the measurement of the response of the full skull surface would be beneficial for further analysis (Dobrev *et al.*, 2017).

Levels of vibration of the cochlea (promontory) in cadaver heads have been shown to be similar to those measured in the live human (Eeg-Olofsson *et al.*, 2013). However, large interindividual variations in the correspondence between the level of vibration and hearing perception have been reported. This may have been due in part to the use of velocity measurement systems with only one sensitivity axis (Dobrev and Sim, 2018; Dobrev *et al.*, 2019). Thus, the complete 3D motion of the skull needs to be considered in the form of the magnitude and phase of the combined (maximum) velocity vector, as it could be a better descriptor of BC hearing than individual orthogonal components (Dobrev and Sim, 2018).

In general, further research has been needed to define the dependence of bone conduction transmission on the location of stimulation (Ito *et al.*, 2011; Stenfelt, 2012; Röösli *et al.*, 2016; Sim *et al.*, 2016). In addition, while finite element (FE) models (Chang and Stenfelt, 2019) simulating the complex interaction between a BCHA and the skull have been verified against single-point measurements, there is still a need for verification using full-field velocity data across the skull surface. Thus, the overall goal of this study was to investigate sound propagation across the skull surface following BC stimulation including specific analyses of (1) 3D motion of the head's surface, (2) its spatial composition, and (3) its dependence on stimulation location. Our hypothesis was that the mode of sound propagation on the skull surface is frequency dependent such that at high frequencies (>1 kHz) there is significant contribution from both normal and tangential components.

II. METHODS

This study was approved by the Ethical Committee of Zürich (KEK-ZH-No. 2012-0136).

A. Measurement procedure

The experiments were conducted on five Thiel embalmed (Thiel, 1992; Guignard *et al.*, 2013) whole head cadaver specimens in the age range of 51–83 years (1 female, 4 males). For each head, two stimulation locations [Fig. 1(A)] were tested: (1) mastoid at a position typical for clinical audiometry, where the actuator is oriented approximately along the left-right direction, normal to the local skull surface; (2) forehead, in the midline 5 cm above the root of the nose, where the actuator is oriented approximately along the anterior-posterior direction, normal to the local skull surface. For both stimulation positions, a 5-N steel band was used for coupling of the actuator to the skin's surface (Håkansson *et al.*, 1986; Mattingly *et al.*, 2015; Chang and Stenfelt, 2019). The electromagnetic actuators from commercial BCHAs (Baha® Cordelle 2 and Baha 5 SuperPower) were used to provide a stepped sine stimulus in the range of 0.1–10 kHz. Under each condition, the response of the skull was monitored as motions of ∼200 points across the ipsilateral, top and contralateral skull surface. In order to reduce possible short and long-term drifts in the response of the Thiel-preserved cadaver heads (Guignard *et al.*, 2013), the duration of the measurement of a single stimulation condition was kept within 2–3 h and total measurement time for all conditions was kept to 2–4 days.

B. Sample preparation

Overall sample preparation was done in a similar way to Dobrev *et al.* (2017). Discussion of the choice of sample preparation and their temporal stability over the length of the experimental sessions is included in Sec. IV A. To provide high optical reflectivity for all three LDV beams across the measured skull surface, retro-reflective glass microspheres (30–100 μm in diameter, P2453BTA-4.2 30–100 μm, Cospheric LLC, CA, USA) were adhered to the skull bone's surface with a thin layer of hair spray (any commonly available brand is acceptable). Before application of the retro-reflective glass microspheres (beads), the skull surface area was cleaned of fat and soft tissue and dried with cotton. Additionally, heads were allowed to

https://doi.org/10.1121/10.0000933

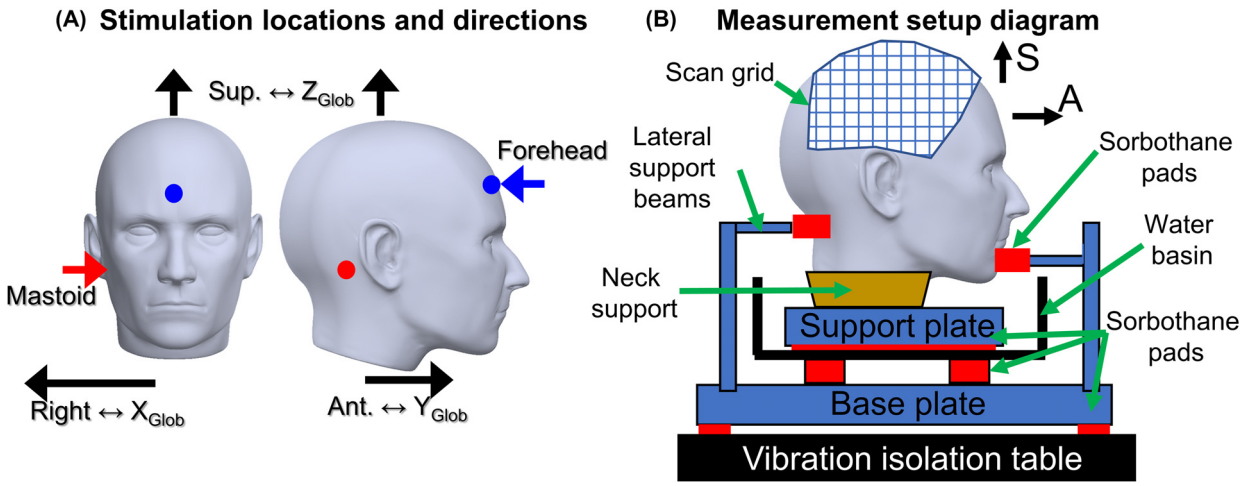

FIG. 1. (Color online) Overview of stimulation direction and location (A); head support and scan area (B). Noted is the correspondence between the anatomical direction and the global (Glob) coordinate system used for data representation. Abbreviations: Ant. is anterior; Sup. is superior.

warm up to room temperature for 1–2 h once taken out of refrigeration in order to reduce any condensation on the bead's surface.

At both stimulation locations, static coupling forces for the 5-N steel band were controlled with a spring gauge (10 N range, 0.1 N accuracy, Light Line, Pesola, Switzerland). While skin was removed from the upper sections of the skull, the skin around the mastoid and neck was left intact. In these areas the skin thickness (including both skin and subcutaneous tissues) varied from 4 to 9 mm, which is in the range for skin thickness recommended for Baha Attract (Mattingly *et al.*, 2015).

C. Measurement setup

A custom head support setup was developed to provide unobstructed optical access to most of the lateral surfaces of the skull, while mimicking the natural orientation and support of the human head [Fig. 1(B)]. The cadaver heads were oriented in an upright position similar to Dobrev and Sim (2018). With this configuration, most of the head's weight was supported by the remaining spine, consisting of C1 to C4. For additional support, to prevent tipping of the head and potential orientational drift during one measurement session (i.e., 2–3 h), the cadaver heads were supported near the skull base with four stiff metal rods (12-mm diameter stainless steel) with sorbothane tips, providing gentle (< 5 N per rod) lateral support. This was especially relevant for measurements at lower frequencies (below 0.5–1 kHz), where head motion is heavily dependent on support (boundary) conditions (Hoyer and Dortheide, 1983; McKnight *et al.*, 2013; Dobrev *et al.*, 2017). The skull contents were left intact, however, there were no measures taken to ensure that there were no air pockets in the skull vault, which could have affected the skull response.

For each stimulation condition, the response of the skull was monitored as motion of the ipsilateral, top, and contralateral skull surface (Fig. 2). Surface motion was quantified by sequentially measuring the velocity of ∼200 points on the skull surface (∼15–20 mm pitch) via a three-dimensional (3D) laser Doppler vibrometer (LDV) system (3D CLV 3000, Polytec, Germany). The unique position and orientation of the 3D LDV at each measurement location was controlled and monitored via the robotic arm (KR 16, KUKA, Germany) [Fig. 2(A)]. The orientation of the 3D LDV was visually adjusted to be approximately normal to the surface. The adjustment was done manually based on visual observation, because head shape data were not available before the measurements. In addition, in order to reduce total measurement time, the LDV orientation was adjusted only per groups of points, as new sections of the skull where being scanned. This approach reduced the measurement time 2–5 fold, while incurring only 5% data loss, due to oblique measurement angle at skull surface sections with high curvature.

The actuators of a Baha® Cordelle 2 (for head 1) and Baha 5 SuperPower (for heads 2–5) (Cochlear Limited, Australia) were used for excitation for both measurement conditions. In all stimulation cases and devices, coupling was provided via the 5 N steel band. The actuators were modified to allow for direct electrical stimulation from the analog output of a data acquisition device (DAQ) (NI-4431, National Instruments, USA) via an audio amplifier (RMX 850a, QSC, CA, USA). For each experimental condition, a frequency stepped sinusoidal stimulus was applied to the BC actuator at 11 frequencies in the range of 0.1–10 kHz: 0.1, 0.25, 0.5, 1, 1.5, 2, 3, 4, 6, 8, and 10 kHz. The stimulus at each frequency was presented continuously for 200 ms with a sinusoidal-shaped ramp up (onset) region of 20 ms and a constant stimulation voltage of 1 Vrms. Both actuators were tested against an artificial mastoid (type 4930, Brüel & Kjær, Denmark), where they exhibited a resonance at 400–500 Hz, with a peak force output of approximately 1 N, and no detectable anti-resonances.

The stimulus was provided five consecutive times (iterations) per frequency for averaging purposes. The measurement procedure was repeated sequentially for each

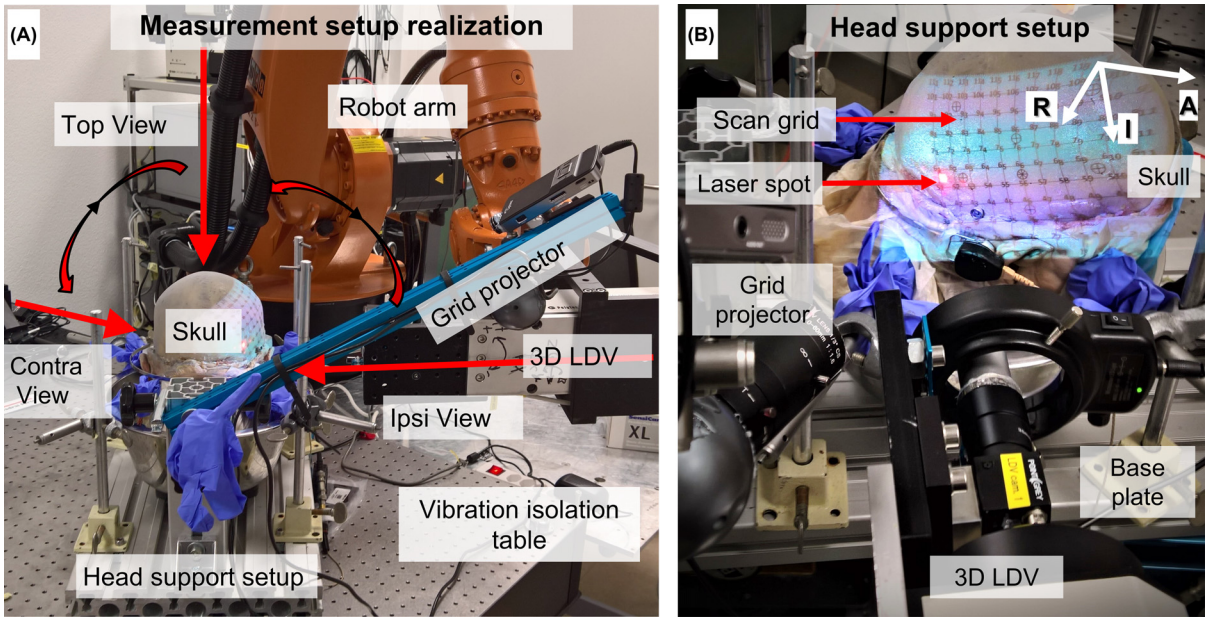

FIG. 2. (Color online) Overview of experimental setup: (A) robot holding the 3D LDV relative to the cadaver head, which is held by the custom head support setup; (B) scan area, with scan grid projected onto the skull surface, as well as the current location of the 3D LDV laser spot and the Baha actuator at the mastoid held via 5 N steel band.

measurement point, resulting in 2–3 h for all measurements (∼200 points) per stimulation condition. The signal generation, motion response recoding and overall automation was handled via a custom-made MATLAB script (MATLAB 2018a, MathWorks, MA, USA). Each stimulus tone was digitally synthesized as a sinusoidal waveform and output via the analog output channel of the DAQ at 192 kS/s and 24 bit of temporal and amplitude resolution, respectively. The DAQ output is them amplified and send directly to the actuator, bypassing the sound processor circuitry.

D. Coordinate systems

Within this work, three coordinate system (Fig. 3) areas were used: (1) LDV; (2) global; (3) local. The **LDV** coordinate system was defined by the 3D LDV system, where $\mathbf{Z_{LDV}}$ is along and $\mathbf{X_{LDV}}$ and $\mathbf{Y_{LDV}}$ are perpendicular to the optical axis of the system. The position and orientation of the **LDV** coordinate system were known for each point, based on the coordinates of the robot arm and calibration of the LDV to the robot (Zhuang *et al.*, 1994; Yaniv, 2015). However, the relative orientation of the **LDV** coordinate

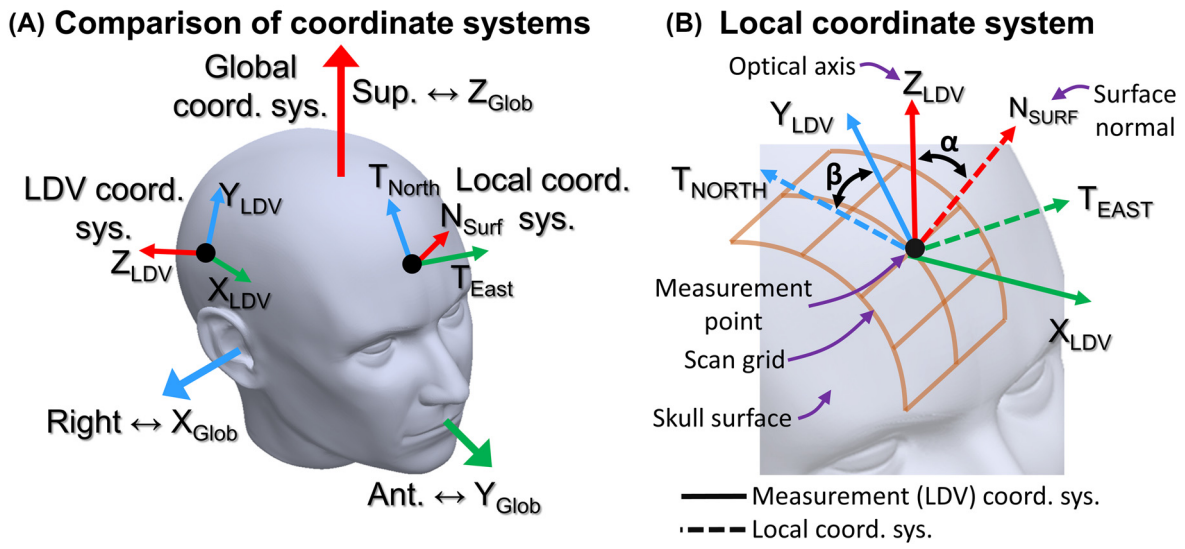

FIG. 3. (Color online) Overview of coordinate systems: (A) anatomical, LDV, local, and global coordinate systems; (B) graphical definition of the local coordinate system, based on the local surface normal and tangents. Included is the angle α, between the unit vectors of the optical axis (Z_{LDV}) and the surface normal (N_{SURF}), and the angle β, between the unit vectors of the LDV Y-axis (Y_{LDV}) and surface tangent in the direction north (T_{NORTH}). Abbreviations: Ant. is anterior; Sup. is superior.; Coord. Sys. is coordinate system; Loc. is local.

https://doi.org/10.1121/10.0000933

system could be arbitrary relative to the head or any relevant anatomical direction or feature, thus hindering comparison between measurement points. To overcome this, the velocity data were transformed into global and local coordinate systems. The global (**Glob**) coordinate system was aligned with the primary anatomical axis, such that: positive $\mathbf{Z_{Glob}}$ was pointing superiorly; positive $\mathbf{Y_{Glob}}$ was pointing posteriorly; and positive $\mathbf{X_{Glob}}$ was pointing to the right (Fig. 3A). The center of **Glob** was at the center of a sphere, which had been fitted (Yd, 2015; McKnight *et al.*, 2013) to the point cloud of measurement points. The **Glob** was used to express either motion of the whole head, such as rigid body motion (RBM) or the predominant direction of motion for the whole surface. The individual axes of **Loc** were defined as: $\mathbf{N_{SURF}}$, pointing laterally along the local surface normal (assuming a convex surface); $\mathbf{T_{NORTH}}$ and $\mathbf{T_{EAST}}$, surface tangents pointing towards the north pole and eastwards, respectively, relative to the sphere fitted to the measurement locations (Fig. 3B). The **Loc** provided the means to express the longitudinal (in-plane deformation) and transverse (out-of-plane deformation) motion locally at each measurement point on the skull surface (Dobrev *et al.*, 2017; Khaleghi *et al.*, 2015).

The spatial transformation from **LDV** to **Glob** was defined based on two consecutive rotations. First, a rotation was applied from $\mathbf{Z_{LDV}}$ to $\mathbf{Z_{Glob}}$, based on the angle between the two corresponding unit vectors (Rodriguez, 1840; Khaleghi *et al.*, 2015; Dobrev *et al.*, 2017). Next, a rotation around the $\mathbf{Z_{Glob}}$ was applied based on the angle between the $\mathbf{Y_{LDV}}$ (in its intermediate orientation after the first rotation) and $\mathbf{Y_{Glob}}$. Essentially, this first rotated $\mathbf{Z_{LDV}}$ to align with $\mathbf{Z_{Glob}}$ and then rotated $\mathbf{Y_{LDV}}$ to align with $\mathbf{Y_{Glob}}$ [Fig. 3(A)]. The spatial transformation from **LDV** to **Loc** (intrinsic) was defined in an equivalent way, such that $\mathbf{Z_{LDV}}$ was aligned with $\mathbf{N_{SURF}}$ with a rotation angle α and $\mathbf{Y_{LDV}}$ was aligned with $\mathbf{T_{NORTH}}$ with rotation angle β [Fig. 3(B)]. It should be noted that the order of rotations matter, as β is the angle between the vectors $\mathbf{Y_{LDV}}$ and $\mathbf{T_{NORTH}}$, after the rotation with angle α is applied to align $\mathbf{Z_{LDV}}$ and $\mathbf{N_{SURF}}$. The surface normal unit vector, unique for each measurement point, was obtained from the shape of the skull, which in turn was obtained by fitting a 2D surface to the point cloud of the measurement points' positions (Dobrev *et al.*, 2017).

E. Estimation of rigid body motion contribution

The motion across the surface of the cadaver heads was approximated as a combination of two spatial "modes" of vibration (Stenfelt, 2011): (1) a pure rigid body motion (RBM) with no relative motion (deformation) between individual points and (2) motion resulting in local deformation, due to relative motion between individual points. The RBM is estimated by fitting a rigid body motion model to the data, accounting for both the 3D velocity and spatial location of each point in an equivalent way to previous publications (Stenfelt *et al.*, 2004; Sim *et al.*, 2010; Dobrev *et al.*, 2017).

In order to differentiate between the two modes, the dissimilarity between the measured motion and the calculated (fitted) RBM was estimated for each measurement point and averaged across all points on the skull surface. This dissimilarity is referred to as RBM fit error (Dobrev *et al.*, 2017) within this work and is used as a method to quantify the extent, to which the cadaver head undergoes pure rigid body motion only, or local deformation. The RBM fit error is quantified using two metrics: (1) the ratio of the RBM fit and the measured motion and (2) the normalized difference of the RBM fit and the measured motion. The ratio metric is defined as the magnitude of the complex ratio between the measured motion and the RBM fit prediction at each point. The normalized difference metric is based on the difference between the measured motion and the RBM fit prediction at each point. The resulting difference is then normalized by magnitude of the combined measured motion at the particular point in order to scale its significance relative to the total observed motion (Dobrev *et al.*, 2017). The ratio and normalized difference are equivalent to the "relative velocity" and "differential relative velocity," respectively, used by Stenfelt *et al.* (2002), however, applied on 3D velocity data—one measured and one fitted.

All calculations were done individually for each motion component, including the combined motion. While both metrics were calculated per point, the final analysis was done based on their average value across points, expressed in the global coordinate system.

F. Combined spatial motion vector

At each measurement point, all three Cartesian components of the velocity were measured, and the combined velocity, $\mathbf{V_{COMB}}$, was calculated based on methods described previously (Dobrev *et al.*, 2017; Dobrev and Sim, 2018). The $\mathbf{V_{COMB}}$ is calculated as the maximum of the instantaneous vector sum of all three orthogonal velocity components, such that it accounts for not only their magnitudes, but also their phase and direction. The $\mathbf{V_{COMB}}$ phase corresponds to the time of the vibration cycle when the vectoral sum of the instantaneous magnitudes of the orthogonal components (instantaneous vectoral sum) reaches a maximum (the $\mathbf{V_{COMB}}$ magnitude), at which point in time, the vectoral sum points in a certain direction (the $\mathbf{V_{COMB}}$ direction). The $\mathbf{V_{COMB}}$ is similar to the commonly used quadratic summation of the magnitude of all three orthogonal components (Stenfelt and Goode, 2005b), however, the quadratic summation could overestimate the maximum velocity at a point, as it assumes no phase delay between the components. As such, the quadratic summation provides an upper bound for the magnitude of the $\mathbf{V_{COMB}}$, while the actual magnitude could be lower depending on the phasing between the orthogonal components (Dobrev and Sim, 2018).

From a physiological perspective, the combined velocity is indicative of the total vibratory motion and it corresponds total kinetic energy at a given measurement point, regardless of measurement direction and coordinate system (Dobrev and Sim, 2018; Stenfelt and Goode, 2005a). In addition, the combined velocity was assumed to be a better representation of the perceived sound (i.e., closer to hearing

sensation), compared to any of the individual components alone (Stenfelt and Goode, 2005a). Because of that, the combined velocity was used to estimate the contribution of the individual orthogonal (elementary) motion components in the global and local coordinate systems, for both the measured motion and the RBM fit. The individual contribution was defined as the magnitude of the complex ratio between each orthogonal component relative to the combined velocity, at each point and on average across the skull surface.

G. Data processing

To reduce effects from random external disturbances, such as LDV signal drop, measurements at each frequency were repeated five times. Several types of quality checks were applied to each data set (five iterations) at each frequency to determine which data were to be further used, equivalent to Dobrev *et al.* (2019). Considerations included the signal-to-noise ratio (SNR), amplitude repeatability, and coherence. The SNR was used to remove responses that were too weak for the LDV to detect reliably. The amplitude repeatability was used to remove individual iterations with potentially erroneous data, possibly due to temporary drop in LDV signal. The coherence was used to remove data, which might have been affected by random external excitation sources. The coherence calculation was based on the magnitude-squared coherence provided by the function "mscohere" in MATLAB 2018a (MathWorks, MA, USA). After the application of all data quality criteria, the remaining data (if available) were reduced to one averaged data point (complex number) per frequency.

The mechanical point impedance at the stimulation locations and the corresponding actuator force out was not measured across the heads. Thus, corresponding raw motion data were normalized by the driving voltage of the actuator. This could have introduced potential variations in the actuator's force output at different locations and coupling types. However, all data analysis within this work was based on normalized values of contribution or spatial patterns of vibration, which were assumed to be independent of stimulation level.

The $\mathbf{X_{LDV}}$ and $\mathbf{Y_{LDV}}$ axes of the 3D LDV system utilized in this work had intrinsically lower (15–25 dB) SNRs compared to the $\mathbf{Z_{LDV}}$ (Dobrev *et al.*, 2018). In addition, the skull response at some locations was up to 30 dB lower than the averages shown in Fig. 4, specifically above 2 kHz. The combination of these two properties could result in greater than 30% data loss in the $\mathbf{X_{LDV}}$ and $\mathbf{Y_{LDV}}$ axes of the 3D LDV system across the surface of the head. While this phenomenon did not compromise the analysis (e.g., motion composition, RBM fit) and discussion of the averaged data across all measurement points, it could have compromised the visual representation of the spatial distribution of the combined velocity or any velocity component across the skull surface, expressed in any of the considered coordinate systems. In order to avoid this problem, all spatial plotting of surface velocity data was based on the raw data from the $\mathbf{Z_{LDV}}$, without any transformation. This was considered sufficiently accurate representation of the surface motion. More details on this method are shown and discussed in Secs. III C and IV A.

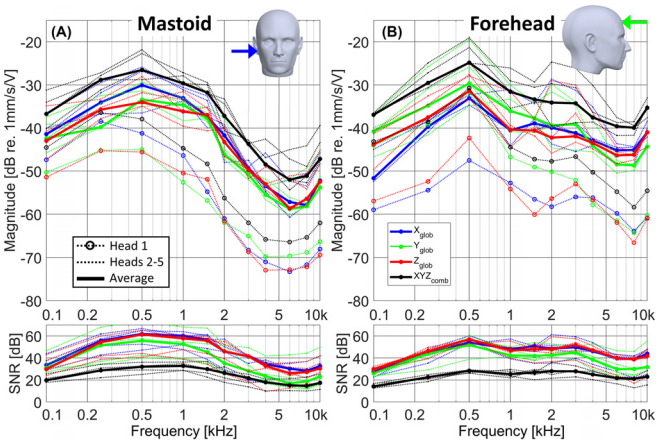

FIG. 4. (Color online) Average response of all measurement points (N = 170–210) across the skull bone surface of all heads (N = 5) for mastoid (A) and forehead (B), expressed in a global coordinate system. Corresponding average SNR for each stimulation condition is included. Figure inset illustrates stimulation direction.

All processing, analysis and data representation was done via custom MATLAB scripts (MATLAB 2018a, MathWorks, MA, USA).

H. Statistical methods

The statistical analysis was done in an equivalent way to Dobrev *et al.* (2019). A paired-sample t-test (two-tailed) was used to estimate the statistical significance of the differences in the averaged magnitude response as a result of any two measurement parameters (e.g., stimulation location, motion components) within a specific frequency range. In addition, the confidence interval for difference between any two measurement data sets was estimated based on the assumption of a normal distribution, which was tested with a Lilliefors test (Lilliefors, 1967). A p-value of <0.05 was used as a threshold for statistical significance for all tests.

The averaged response, named "frequency-average," at each frequency and each test condition was calculated by averaging the complex values of the velocity across measurements points across the skull surface individually for each motion component in each coordinate system. Thus, the velocities of all 150–220 measurement points (depending on measurement condition and data quality) across the skull surface were represented by one number for each measurement frequency, motion component (3 per system + 1 combined), coordinate system (global or local), and measurement condition (mastoid or forehead stimulation). In the case of data normalized by the combined motion, individual motion components were normalized before calculation of the frequency-average of all points.

Since only five samples were available for this study per frequency point, data at all frequencies within a

https://doi.org/10.1121/10.0000933

specified frequency band were used for comparison. This metric was named "band-average" (Dobrev *et al.*, 2019). There were four frequency bands under consideration, low (0.1–0.5 kHz), low-mid (0.5–1.5 kHz), mid (1.5–4 kHz), and high (4–10 kHz). The choice of the specific band limits was guided by preliminary analysis and observations of the collected data, and different trends in each band.

Since the band-average was a single value for each band, it was plotted as a flat line within each band, the length of which represented the width of the band. An upper and lower bound for a 95% confidence interval was calculated based on the average (median) response of each individual sample within the specific frequency band. Statistical significance ($p < 0.05$) of the difference between any two measurements was marked with an "o" on the center of the band.

It should be noted that no adjustment was applied for the use of multiple t-tests (used $\sim$ 200 times across the data set). Due to the small sample size ($n = 5$), no further statistical analysis or corrections were done. Thus, the uncorrected t-test results were used to indicate potential trends rather than rigorous statistical proof of significant difference.

III. RESULTS

A. Average skull response and direction

1. Average response of the skull bone's surface

Figure 4 illustrates the averaged response and corresponding SNR of all measurement points ($N = 170$–220) across the skull surface for stimulation at the mastoid and forehead. The averaged response is expressed as the three individual (elementary) orthogonal components and the combined motion in the global coordinate system. Each graph contains both the average of all heads (thick lines) as well as the individual responses (thin lines). This figure provides an overview of the raw data before any normalization or RBM fitting showing the general frequency behavior of the two stimulation locations, as well as the SNR.

The first sample (head 1) was stimulated with the Baha Cordelle 2 actuator. For the rest of the samples, a Baha 5 SuperPower actuator was used. This difference in stimulation devices caused the raw (non-normalized) response of head 1 to be 10–20 dB lower than the rest of the heads, resulting in a drop of the SNR for some components to below 20 dB > 3 kHz. This is illustrated in Fig. 4, where head average curves are based on the data of heads 2–5 only. This separation is done only in this figure, while data from all heads were included in the statistics throughout the rest of this work. Regardless of the difference in actuators, all samples followed a qualitatively similar trend with frequency.

2. Predominant motion direction

The predominant head motion, under each stimulation condition, was estimated based on the contribution (i.e., complex ratio) of the individual motion components to the total (combined) motion. This approach compensated for variation in the frequency dependent response of the BCHA actuator across heads. The contributions at each point were then averaged across points. The averaged contribution and its 95% confidence interval per frequency band (see Sec. II H for details) of each motion component was calculated for both stimulation conditions and expressed in global [Figs. 5(A) and 5(B)] and local [Figs. 5(C) and 5(D)] coordinate systems.

For mastoid stimulation below 1 kHz [Fig. 5(A)], the $\mathbf{X_{Glob}}$ component, which was along the stimulation direction, had a 2–8 dB larger (95% confidence interval) contribution than did the other orthogonal components. The $\mathbf{Y_{Glob}}$ and $\mathbf{Z_{Glob}}$ components had approximately the same contributions. For forehead stimulation below 1 kHz [Fig. 5(B)], the $\mathbf{Y_{Glob}}$ component had a 2–16 dB larger contribution than the $\mathbf{Z_{Glob}}$, and a 3–20 dB larger contribution than the $\mathbf{X_{Glob}}$ components. This was consistent with the stimulation direction's being approximately along the $\mathbf{Y_{Glob}}$ axis, as shown in Fig. 1(A). However, the predominance of the motion along the stimulation direction was not statistically significant for any of the stimulation locations. Above 2 kHz, all

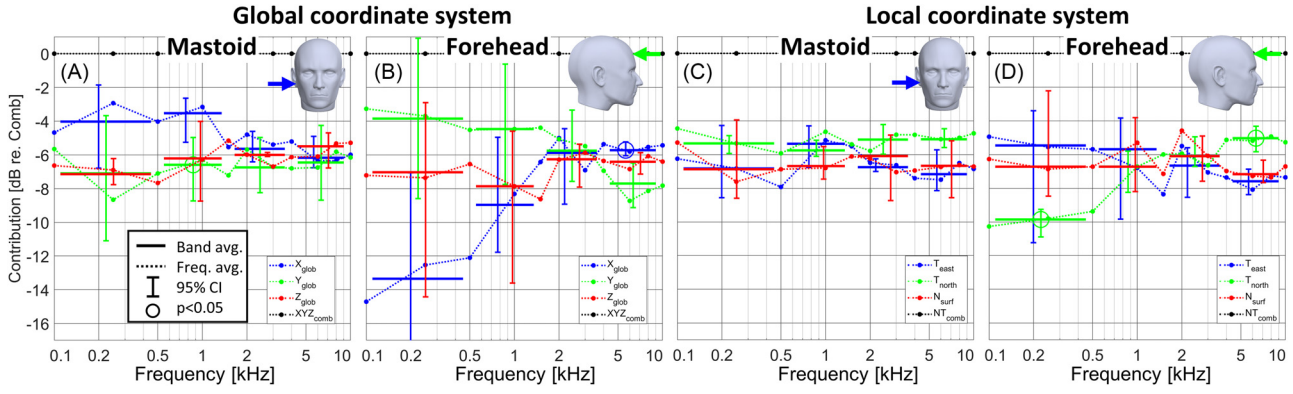

FIG. 5. (Color online) Averaged contribution of each orthogonal motion component of the skull bone surface motion for mastoid [(A), (C)] and forehead [(B), (D)] stimulation, expressed in a global [(A), (B)] and local [(C), (D)] coordinate systems. Figure inset illustrates stimulation direction. Abbreviations: Comb. is combined motion.

components had approximately similar (within 1–3 dB difference on average) contributions for both stimulation locations.

For mastoid stimulation, the contribution of all motion components in the local (**Loc**) coordinate system was within 1–3 dB of each other overall for all frequencies. For stimulation on the forehead below 0.5 kHz, the surface tangent component, $\mathbf{T_{NORTH}}$, was 3–10 dB smaller relative to the other components (statistically significant relatively to $\mathbf{N_{SURF}}$). However, the contribution of the tangential component $\mathbf{T_{NORTH}}$ increased with frequency, reaching a statistically significant predominance of 0.5 to 4 dB above 4 kHz, relative to the other two components.

B. Rigid body motion (RBM)

1. How well did low frequency motion fit to RBM?

Figure 6 displays the relation between the rigid-body-motion (RBM) fit and the measured motion, expressed in three different ways in the global coordinate system. The left column of Fig. 6 [panels (A) and (D)] displays a comparison of the average (across points) of the measured motion and RBM fit for the individual components and the combined motion. Deviation between any of the corresponding components would indicate deformations in the corresponding direction. The middle column [panels (B) and (E)] represents the ratio of the RBM fit versus the measured motion, for the individual motion components. In this case, the presence of deformations would be indicated by a ratio that was significantly different from 0 dB (e.g., ratio of 1), indicated visually as a thick black dashed line (threshold). The right column [panels (C) and (F)] displays the normalized difference (see Sec. II E) between the RBM fit and the measured motion. In this case, the presence of deformations would be indicated by values approaching 0 dB. For this metric, a threshold of −6 dB (indicated visually as a thick black dashed line) was selected as an indicator for a sufficiently small error for RBM fit. Details on the reasoning behind selecting these threshold values is given in Sec. IV C.

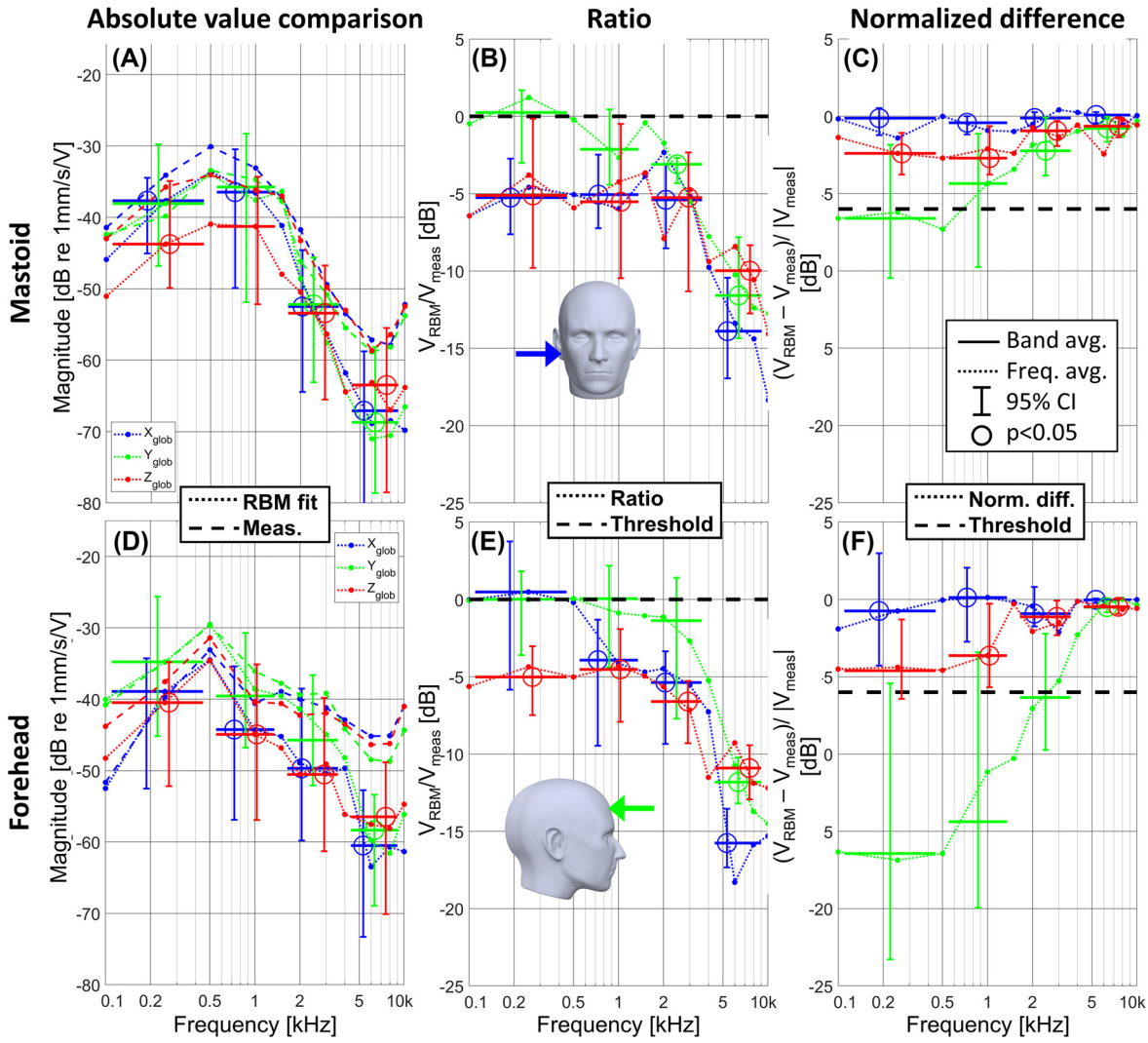

FIG. 6. (Color online) Comparison of the rigid body motion (RBM) versus the measured motion across the skull surface for the forehead (top row) and the mastoid (bottom row) stimulation, in global coordinate system. The comparison of each orthogonal component and the combined motion is expressed as (A, D) absolute value comparison; (B, E) magnitude of the complex ratio; (C, F) normalized difference. Figure inset illustrates stimulation direction. Abbreviations: Meas. is measurement; Norm. diff. is normalized difference.

https://doi.org/10.1121/10.0000933

For mastoid stimulation [Fig. 6(A)] below 1.5 kHz, the RBM-fit differed from the measured motion along the $\mathbf{X}_{\mathbf{Glob}}$-axis (presumed stimulation direction) at all frequencies. In contrast, the RBM-fit matched the data better (no statistical difference below 1 kHz) along the $\mathbf{Y}_{\mathbf{Glob}}$, perpendicular to the stimulation direction. At higher frequencies, all components of the RBM fit were significantly lower (9–17 dB) than the measured motion.

For forehead stimulation below 1.5 kHz [Fig. 6(D)] (presumed stimulation direction is along the $\mathbf{Y}_{\mathbf{Glob}}$-axis), the $\mathbf{Y}_{\mathbf{Glob}}$ component (approximately along the stimulation direction) was dominant and nearly identical (<1 dB deviation) to the average response for both RBM fit and measured motion. At higher frequencies, the RBM underestimated the measured motion by up to 9–17 dB, for both stimulation locations.

Figures 6(B) and 6(C) indicated similar trends, where for mastoid stimulation above 1.5 kHz, both the ratio and normalized difference metrics had significant deviations from RBM for all motion components. At lower frequencies, only the $\mathbf{Y}_{\mathbf{Glob}}$ component did not indicate significant difference from RBM. Similarly, for forehead stimulation below 1.5 kHz [Figs. 6(E) and 6(F)], only the $\mathbf{Y}_{\mathbf{Glob}}$ component showed no significant difference from the 0-dB ratio and an average of −17 to −10 dB normalized difference, significantly below the −6-dB threshold.

2. RBM composition

Figure 7 is a detailed display of the composition of the RBM relative to the combined motion. The RBM consists of three translational (T_X, T_Y, T_Z) and three rotational (ω_X, ω_Y, ω_Z) components. The three translational components describe the common velocity of all points on the surface and define the motion of the geometrical center of the "body" of points, along a corresponding orthogonal axis in the global coordinate system. For example, T_X is linear velocity component of the RBM motion, common for of all points of the "body," along the global X-axis. The three rotational components describe the motion of the body of points around the corresponding axis of rotation, for a

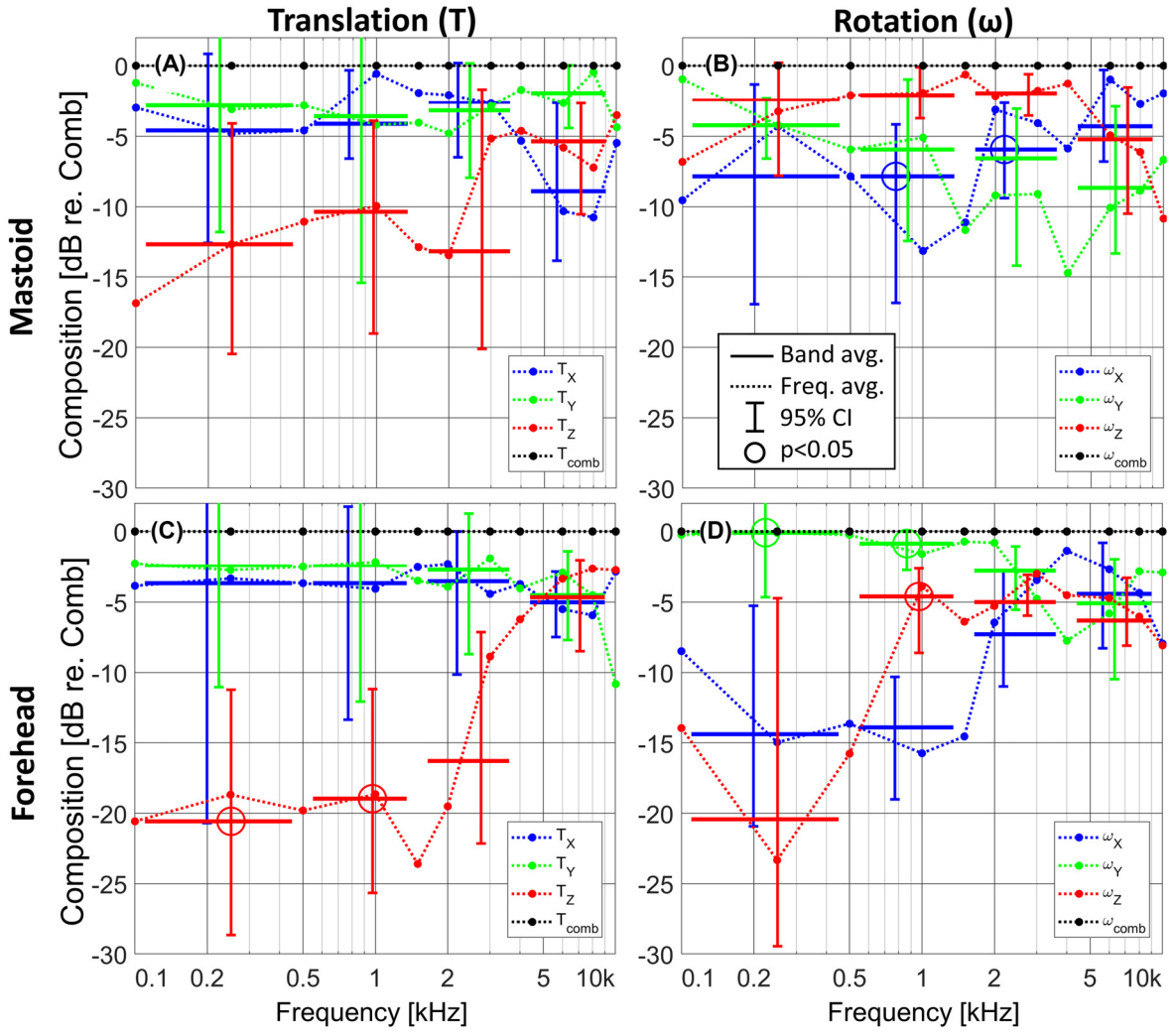

FIG. 7. (Color online) Motion composition of the rigid body motion (RBM), expressed as the magnitude of the complex ratio of the translational (T) (A, C) and rotational (ω) (B, D) motion components, normalized by the corresponding combined motion. Stimulation was provided at the mastoid (A, B) and the forehead (C, D).

coordinate system at the geometrical center of all measured points, which is aligned with the global coordinate system. For example, ω_X is the rotational velocity component of the RBM motion of all points around an axis at the center of the "body" of points, parallel to the global X-axis. Further details of the RBM definition area provided by Sim *et al.* (2010). Statistics were based on comparison of any component with its corresponding combined motion. Based on the predominant trend of the RBM fit error, as shown in Fig. 6, only data below 1.5 kHz in Fig. 7 were considered for discussion purposes.

Under mastoid stimulation [Figs. 7(A) and 7(B)], the samples exhibited a trend for predominant T_Y and T_X translation, corresponding linear motion along the $\mathbf{Y_{Glob}}$ and $\mathbf{X_{Glob}}$ axes, which was approximately along the stimulation direction. The resultant rotational motion had a predominant ω_Z component, corresponding to rotation around the $\mathbf{Z_{Glob}}$ axis, with comparable (within 1–5 dB) contribution from all rotation axis.

Under forehead stimulation [Figs. 7(C) and 7(D)], the samples exhibited a predominant $\mathbf{Y_{Glob}}$ translation, T_Y, with a comparable (within 1–3 dB) contribution from the $\mathbf{X_{Glob}}$ translation, T_X. The resultant rotational motion was dominated by ω_Z component, corresponding to $\mathbf{Y_{Glob}}$-axis rotation, being 15 dB higher than the other two rotational components below 0.5 kHz.

C. Surface wave pattern with varying stimulation location

1. Correlation between Z_{LDV} and V_{COMB}

In order to maximize the skull surface coverage in the analysis of the surface motion, while utilizing data with sufficiently high SNR, $\mathbf{Z_{LDV}}$ (in the raw LDV coordinate system) was used to express the surface response at and above 2 kHz, instead of the combined motion at each point, $\mathbf{V_{COMB}}$. This was done because $\mathbf{Z_{LDV}}$, of the 3D LDV system, had a 15–25 dB lower noise floor (Dobrev *et al.*, 2019) than the other two components, thus resulting in the highest number (>90% versus 50%–80% for the other two components) of points with good SNR. The similarity between the $\mathbf{Z_{LDV}}$ and $\mathbf{V_{COMB}}$ was estimated based on the average of the spatial correlation of the velocity maps, as described by Dobrev (2014). This metric indicated a range of 91%–97% spatial correlation across all heads, with higher values for lower frequencies. Figure 8 is a representative comparison of instantaneous velocity maps at 2, 4, and 8 kHz under forehead stimulation of head 4.

2. Deformation wave patterns at mid and high frequencies

Figures 9 and 10 compare the instantaneous velocity maps across the surface of five skulls for stimulation at the mastoid and forehead, at 2 and 8 kHz. In each velocity map, white dashed lines with arrows indicate the trajectory and direction of the traveling wavefront in the local deformation pattern near the dashed lines. Deformation patterns not marked with white dashed lines correspond to stationary patterns due to local standing waves. For better visualization of the vibration patterns in Figs. 8–10, please refer to the corresponding movies (Mm. 1–3).

Mm. 1. Visual comparison between the motion components in Fig. 8. This is a file of type "mp4" (8.6 MB).

Mm. 2. Skull surface motion maps for mastoid stimulation in Fig. 9. This is a file of type "mp4" (10 MB).

Mm. 3. Skull surface motion maps for forehead stimulation in Fig. 10. This is a file of type "mp4" (10.1 MB).

Within Figs. 9 and 10, the cadaver heads (CH) are referred by numbers 1–5, such that, for example, CH1 stands for cadaver head 1. For mastoid stimulation at 2 kHz (Fig. 9, left column), there was a common spatio-temporal behavior of the deformation pattern across the ipsilateral (right) side, in all heads. The pattern consisted of 2 local extrema (alternating between maxima and minima) forming a traveling

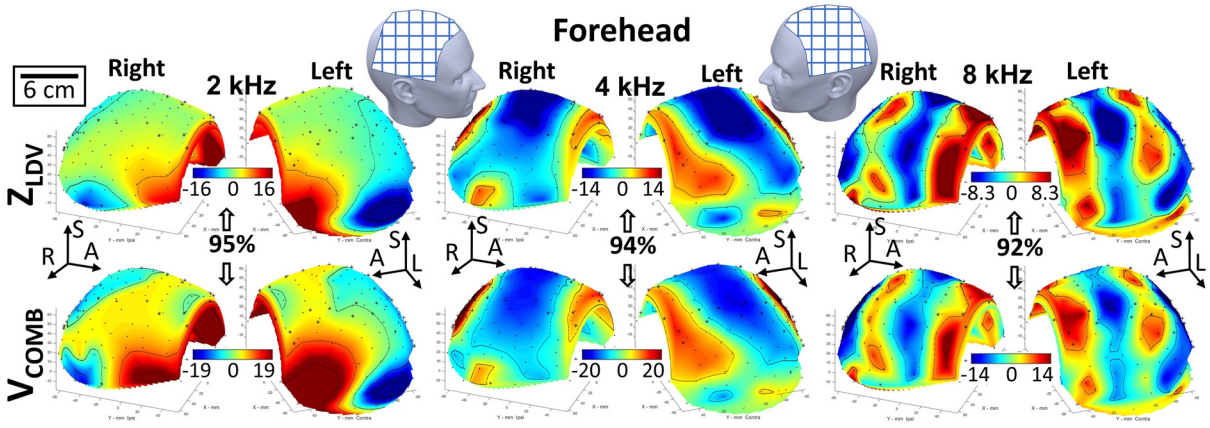

FIG. 8. (Color online) Visual comparison between the $\mathbf{Z_{LDV}}$ (in raw LDV coordinate system) and $\mathbf{V_{Comb}}$ (combined motion) based on the instantaneous velocity map at 2, 4, and 8 kHz for forehead stimulation, including corresponding spatial correlation values. Figure insets illustrate the approximate orientation of the head and scan area in each of the left and right views. Color bars are in units of μm/s/V. See Mm. 1 for video version.

https://doi.org/10.1121/10.0000933

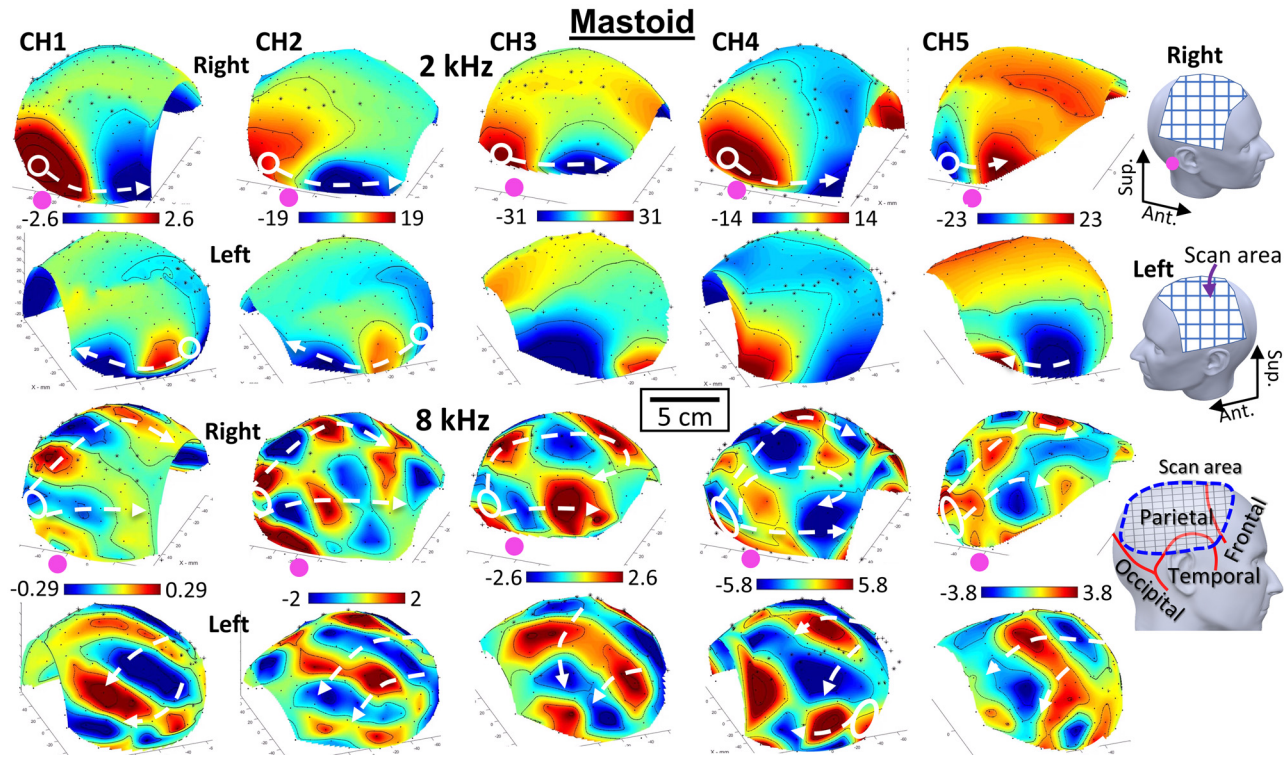

FIG. 9. (Color online) Skull surface motion maps of cadaver heads (CH) 1–5, based on the instantaneous velocity, for mastoid stimulation at 2 and 8 kHz. Indicated are the actuator location (pink dot), the estimated wave origin (white circle), and wave motion direction (white arrows). Figure insets illustrate: (bottom left) the approximate location of the scan (measurement) area relative to the skull plates; (top right) the approximate orientation of the head and scan area in each of the left and right views. Color bars are in units of μm/s/V. See Mm. 2 for video version.

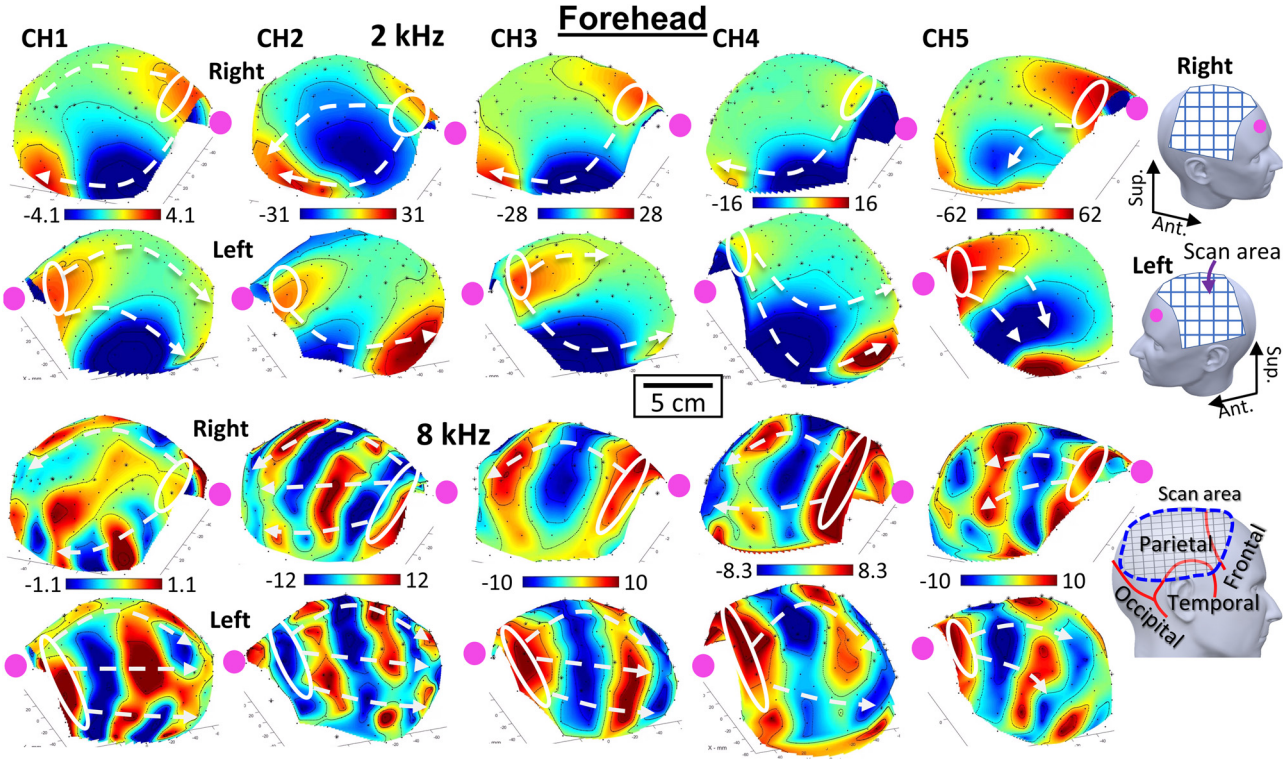

FIG. 10. (Color online) Skull surface motion maps of cadaver heads (CH) 1–5, based on the instantaneous velocity, for forehead stimulation at 2 and 8 kHz. Indicated are the actuator location (pink dot), the estimated wave origin (white circle), and wave motion direction (white arrows). Figure insets illustrate: (bottom right) the approximate location of the scan (measurement) area relative to the skull plates; (top right) the approximate orientation of the head and scan area in each of the left and right views. Color bars are in units of μm/s/V. See Mm. 3 for video version.

wave originating from the posterior-inferior part of the skull, approximately around the interface between occipital and parietal bones. The wavefront then travelled anteriorly, deforming primarily the inferior half of the skull (inferior parts of the parietal and superior part of the temporal bones), with some activation of the anterior-superior sections, approximately near the interface between parietal and frontal bones. The distribution of the velocity pattern (for mastoid stimulation at 2 kHz) on the contralateral (left) side was qualitatively similar to the ipsilateral (right) side, at least from the spatial distribution perspective. However, on the contralateral side, only head 1 exhibited clear traveling wave behavior from the occipital to the frontal bones, while the other samples showed either a purely standing wave pattern (heads 3 and 4) or a very localized traveling wave pattern (head 2, near the parietal-occipital interface).

For mastoid stimulation at 8 kHz (Fig. 9, right column), the full skull surface was activated, consisting of primarily traveling wave patterns. On the ipsilateral side (right), the wave pattern appeared to originate at a similar location as at 2 kHz, namely, around the interface between occipital and parietal bones. A common behavior of the wave pattern for all heads was a circumferentially travelling wavefront ("wave train") from the interface of the base, occipital and parietal sections on the ipsilateral side (visual origin area), to a diametrically opposing area on the contralateral side, approximately at the interface of the frontal, parietal and temporal bones. A similar "wave train" behavior has been reported by McKnight *et al*. (2013).

The spatial density (distance between neighboring local minimal and maxima) of the 8 kHz deformation patterns (Dobrev *et al*., 2017) varied approximately 10% to 30% between skulls; however, there were also location-dependent variations across each skull. Specifically, local deformations near the wave's origin at the parieto-occipital interface at the posterior-inferior of the ipsilateral side (beginning of the "wave train") and near the parietal-base-frontal interface on the anterior-inferior of the contralateral side (end of the "wave train") showed 50%–100% higher spatial density than across the superior half of the skull. The overall wave speed was estimated to be in the range of 350–450 m/s.

For forehead stimulation at 2 kHz (Fig. 10, left column), there was a travelling wave pattern originating from the anterior-superior part of the skull, around the parietal-frontal interface, moving symmetrically to the left and right sides of the inferior sections of the skull. The deformation pattern on either side of the skull was localized to the inferior sections near the skull base. The wave patterns were qualitatively similar in shape and spatial density to the ipsilateral motion pattern under mastoid stimulation; however, the wave fronts were moving in the opposite direction (anterior to posterior).

For forehead stimulation at 8 kHz (Fig. 10, right column), the full skull surface was activated, exhibiting primarily traveling wave patterns. The wave pattern appeared to originate along the full length of the parietal-frontal interface, travelling posteriorly as a "wave train." The wavefronts appeared axially symmetric around the $\mathbf{Y}_{\mathbf{Glob}}$ axis (anterior-posterior), with the exception of the response of head 1, where the right side showed a less organized pattern than the left due to the presence of wavefronts travelling in other directions. There was a disruption in the pattern of the wavefronts near the interface with the skull base, causing local wave patterns.

The spatial density of the local extrema within the velocity maps for forehead stimulation varied between heads in a similar way as for mastoid stimulation. In other words, heads exhibiting longer wavelengths at 8 kHz under forehead stimulation exhibited similarly longer wavelengths under mastoid stimulation. For example, at 8 kHz for mastoid stimulation (Fig. 9), head 2 vibration pattern exhibits approximately 2.5 wavelengths (i.e., starting from the stimulation location: maxima-minima-maxima-minima-maxima) along a circumference from the stimulation location to the top of the skull. In contrast, under the same stimulation conditions, the head 3 vibration pattern exhibits only 1.5 wavelengths, thus 40% longer wavelength. This ratio of wavelengths between heads 2 and 3, observable within the vibrational pattern, remains approximately the same for forehead stimulation.

IV. DISCUSSION

A. Methodological considerations

1. Choice of samples and their temporal stability

Thiel embalmed heads, instead of fresh heads, were used because a full set of measurements for each head took $\sim$ 2–3 days. This time period would have been too long to assume a sufficiently consistent dynamic response if fresh heads were used, as indicated by previous research (Guignard *et al*., 2013) comparing fresh and Thiel-preserved temporal bones. The test schedule for this study was organized such that the measurement time per measurement condition was kept to 2–4 h. For such a time window, previous work has indicated a potential temporal drift of 1–3 dB with a 5 N steel band coupling (Dobrev *et al*., 2019). However, the range of the measured motions between local extrema across the skull was 20–40 dB, thus much larger than any potential short-term drift. In addition, qualitatively similar wave patterns have been observed previously (Dobrev *et al*., 2017) using measurement times of less than 0.5 h. Thus, it can be assumed that the measured motion patterns were not affected significantly by potential methodological constraints.

The effect of the removal of the skin on the response of the skull surface have been previously explored by Dobrev *et al*. (2017), where a frequency shift downwards in the frequency response, and the transition frequency in particular, was observed. This was potentially due to the added effective damping and mass from the skin. Such downwards shifts have been observed before due to the loading from the contents of the skull in the case of CSF (Dobrev *et al*.,

https://doi.org/10.1121/10.0000933

2016) and gel (Franke, 1956). The overall amplitude of the average response of the skull surface could also have been increased due to the removal of the skin. However, it is hypothesized that these potential changes do not affect in a significant way the conclusions within this work, and the observations would still hold for intact skulls.

2. Skull surface treatment and SNR considerations

During preliminary tests it was found that most of the detectable (>0.5–1 dB) variations in the velocity measurements, within 2–3 mm of a specific location on the skull surface, could be reduced by careful treatment of the skull surface at the measurement area. This included removing all soft tissue and moisture from the surface before applying the retroreflective spheres. The LDV signals from the retroreflectors were maintained in the range of 90%–100% of the maximum for the LDV in order to maximize SNR for all motion components (Dobrev *et al.*, 2019).

Overall, the SNR of all motion measurements deteriorated below 0.25 kHz [Figs. 4(A) and 4(B)], due to the higher mechanical impedance of the skull (Stenfelt and Goode, 2005b). In addition, due to its optical design, 3D LDV system has a higher (15–25 dB) noise floor for $\mathbf{X_{LDV}}$ and $\mathbf{Y_{LDV}}$ than $\mathrm{Z_{LDV}}$. (Dobrev *et al.*, 2019). Overall, low-SNR data did not affect any of the trends and corresponding observations in this work.

3. Validity of the use of a single motion component to visualize surface waves

Qualitative visual inspection as well as quantitative spatial correlational analysis of the data displayed in Fig. 8 indicated a sufficient correlation (92%–95% for head 4, and 91%–97% across heads, at 2–8 kHz) of the spatial pattern and direction of propagation of the surface wave pattern of the $\mathbf{Z_{LDV}}$ and $\mathbf{V_{COMB}}$. In addition, data displayed in Fig. 5, for both stimulation locations, indicated similarity (within 1–3 dB) of the average response of all motion components above 1.5 kHz, in both local and global coordinate systems. Together, these observations support the assumption that using the raw Z-axis output (along the optical axis) only of the 3D LDV system was sufficiently accurate to represent the skull surface motion within the scope of the analysis of this work. This allowed for a greater amount of data with sufficient SNR to be included in the analysis of surface wave patterns. This also supports the validity of the findings from previous work (Dobrev *et al.*, 2017), where most of the available data were from a scanning LDV system with a single sensitivity axis (i.e., only one velocity component).

B. Averaged response of the skull surface

1. Absolute levels of skull motion

Based on the absolute level (raw) data displayed in Fig. 4, at mid and high (>2 kHz) frequencies, the forehead stimulation appeared to activate the skull's surface an average of 7–12 dB greater than mastoid stimulation. Based on the spatial distribution of the deformations in Figs. 9 and 10, specifically at 2 kHz, the stronger response with forehead stimulation was likely due to increased activity of the parietal bones in vicinity of the stimulation location. However, hearing thresholds have been shown to be equal or better for ipsilateral and contralateral mastoid stimulation (Ito *et al.*, 2011) than for forehead stimulation. This suggests that the cochleae are not "directly" excited from the parietal or the frontal bones. This hypothesis is supported by discrepancies in the wave fronts' origins and actuator location observed in wave patterns across the skull surface under mastoid stimulation (Fig. 9). This could suggest that the actuator may be more efficient if implanted at the mastoid in order to provide more direct stimulation of the ipsilateral cochlea (Dobrev *et al.*, 2019). This has been evidenced by recently developed BCHAs (Håkansson *et al.*, 2010; Reinfeldt *et al.*, 2015; Dobrev *et al.*, 2018).

2. Contribution of individual motion components

Evaluation of the contribution of each motion component, relative to the combined motion allows for observation of the intrinsic behavior of the heads without the frequency dependence of the actuator, assuming a linear response of the cadaver heads (Håkansson *et al.*, 1986).

Data displayed in Fig. 5(A) and 5(B) indicate that overall, the head followed the stimulation direction but only at low frequencies (<1.5 kHz), and even then, there was substantial contribution from other components. In the case of mastoid stimulation, the average response along the stimulation direction was only 2–4 dB larger than the other two orthogonal components. This is likely because the stimulation was applied at the base of the head, near the support structure. As indicated by both the current (Fig. 6) and previous work (Hoyer and Dortheide, 1983; McKnight *et al.*, 2013; Dobrev *et al.*, 2017), cadaver head motion at such frequencies is rigid-body-like, thus heavily dependent on support (boundary) conditions. Thus, when stimulation is applied near the support location, the dynamics of the support structure (boundary conditions) has to be taken into consideration and could affect the cadaver head dynamics. Stimulation further away from the base (support) of the head, as is the case with forehead stimulation [Fig. 5(B)], resulted in 3–12 dB greater dominance than for other components of the motion along the stimulation direction. Again, this could be explained as an effect of the specific boundary conditions, where the force of application further away from the support of the sample would result in more deflection from the neutral position. In other words, stimulation further away from the skull base results in lower stiffness, which is the real part of the impedance, as seen by the actuator at lower frequencies.

Further, stimulation at higher frequencies (>1–2 kHz), resulted in an insignificant difference between the individual components of the average response across the skull surface. Such behavior has been previously observed with the measurement of the spatial motion (i.e., all orthogonal

components) of the promontory response (Dobrev *et al.*, 2019; Stenfelt and Goode, 2005b). However, even if a "pure" unidirectional stimulation could be applied, there is no conclusive evidence that any particular direction is optimal for providing significantly stronger transmission for cochlear activation (Chang *et al.*, 2018; Chang and Stenfelt, 2019). This may suggest that stimulation direction of bone conduction hearing aids is not crucial for setting the skull into vibration and thus for hearing, particularly above 1 kHz. Thus, it could be hypothesized that the magnitude of the combined motion and the effects of the relative deformations between the different sections of the skull, between stimulation location and cochlea, are more relevant for cochlear activation than any particular stimulation direction.

The motion composition of the local coordinate system is indicative of the contribution of the local bending and in-plane compression components (Dobrev *et al.*, 2017). Stimulation at the mastoid resulted in a nearly equal (1–3 dB difference) contribution of tangential and normal components that was not frequency dependent. Stimulation at the forehead showed a trend of increasing contribution of the tangential motion (specifically $\mathbf{T}_{\mathbf{NORTH}}$) with frequency. This contradicts previously observed behavior (Dobrev *et al.*, 2017); however, past measurements were done on the superior most section of the parietal bone only, which might not be sufficiently representative of the full skull area as measured in the present study. Nevertheless, both data sets indicate a general trend of comparable contributions from both tangential and normal components above 1 kHz. This trend could be attributed to a potential change in the behavior of the wave motion across the skull surface with increasing frequency. Namely, there is a transition from spherical shell bending, predominantly of the normal components to plate extension waves, predominantly of the tangential components, as suggested by McKnight *et al.* (2013).

Combining observations for the local behavior of the skull and the apparent insensitivity of the skull to the stimulation direction above 1 kHz, it could be hypothesized that radically different types of bone conduction actuators could be designed in the future that stray away from the traditional "piston" action design (e.g., Baha® and Ponto®). Specifically, future actuators could be optimized to induce local (out-of-plane) bending or tangential (in-plane) compression of the skull surface, as suggested by previous work (Adamson *et al.*, 2010).

C. Rigid body motion fit and composition

1. RBM fit

Both RBM fit metrics as well as the absolute value comparison between the RBM fit and the measured data indicated that there is a "transition" frequency (Dobrev *et al.*, 2017; Stenfelt, 2011), above which the motion pattern changes from predominantly rigid motion, with translation and rotation, to predominantly local deformations. The skull surface exhibits this transition frequency between approximately 1–2 kHz, which is comparable to values seen before by surface velocity scans of smaller sections (<10–12 cm diameter) of the skull (0.5–1 kHz reported by Dobrev *et al.*, 2017) as well as the full surface of dry skulls (0.68–0.8 kHz reported by McKnight *et al.*, 2013). However, this transition frequency is higher than the values observed in measurements of promontory motion (0.5–0.6 kHz) (Dobrev *et al.*, 2019) and local impedance at individual points (0.3–0.5 kHz) on the skull surface (Stenfelt and Goode, 2005b). The differences with the local impedance measurements could be attributed to different coupling methods except for the promontory response, which was acquired with equivalent coupling (Dobrev *et al.*, 2019). In this case, discrepancies could be explained by potential differences in the transition frequencies of the upper sections of the skull and the temporal bone containing the cochlea. More detailed discussions on this topic are in Sec. IV D 1. The threshold values for each metrics were defined based on previous experience (Dobrev *et al.*, 2017) and visual (qualitative) correlation with corresponding surface motion patterns.

Even below the transition frequency, the RBM model fitted well to only some of the motion components with significant deformations (<10 dB normalized difference with the measured motion) along other components, independent of stimulation condition. This suggests that the skull could be experiencing deformations along specific directions at lower frequencies than previously expected. One such mode of deformation could be the "mass-spring" mode with predominant deformations along the X-axis (Stenfelt, 2011; McLeod *et al.*, 2018).

2. RBM composition

The composition of the RBM of the heads depends on the stimulation position for low frequencies, as expected from the averaged data displayed in Fig. 6. The predominant direction of motion followed the direction of stimulation; however, there was still significant motion in at least one more direction due to the complicated rotation motions that the heads underwent. This was evident by the limited difference, of only 1–5 dB on average, between the strongest and the second strongest translation motion component below 1 kHz, for both stimulation locations. The resultant RBM rotations did not follow the stimulation direction in a simple manner. For example, for forehead stimulation [Figs. 7(C) and 7(D)], the heads underwent predominantly rotation around the Y axis (15 dB higher than other components below 0.5 kHz), which is parallel to the stimulation direction, instead of perpendicular as expected from the simple case scenario. In the case of mastoid stimulation [Figs. 7(A) and 7(B)], the heads underwent complex rotational motion with comparable (1–7 dB difference) contribution from all components below 1 kHz. Again, this could be attributed to an effect from the support of the heads combined with the close proximity of the stimulation location to the support area at the skull base. In general, stimulation further away from the base resulted in a "purer" rigid-body-like motion below 1 kHz. At frequencies >1 kHz, the RBM fit error

https://doi.org/10.1121/10.0000933

metrics (Fig. 6) indicated significant deformations, evidenced by wave motion (Figs. 9 and 10) as well as a mixed contribution from all components (Fig. 5). Thus, interpretation of the RBM fit at those frequencies was not done.

D. Wave patterns across the skull surface

Analysis of the surface wave patterns on the skull surface at mid and high frequencies allows for quantification of the behavior of various sections the skull under different stimulation conditions. Analysis of such data allows for the evaluation of the direction and speed of the local wave motion for a given actuator location and stimulation direction.

1. Wave origin and plate interaction

Overall, the visually identifiable origin of the wave patterns did not coincide exactly with the location of the Baha actuator for either mastoid or forehead stimulation at any frequency. The wave pattern for the mastoid stimulation (Fig. 9) originated from approximately the anterior part of the interface between occipital and parietal plates; however, this was up to 5–7 cm away from the actuator location. This discrepancy was even more apparent for stimulation at the forehead (Fig. 10), where the wave "origin" appeared to be the whole semi-circumference of the parietal-frontal interface. In both cases, the wave origin was not a localized spot (within one point of the scan grid), but a larger section ($>$5–10 cm^2), approximately at the interface between the skull plates.

Based on these observations, it can be hypothesized that the thicker skull sections (i.e., occipital, temporal, and frontal) exhibit rigid-like motion up to higher transition frequencies. This is supported by previous work indicating significant spatial variation in the effective Young's modulus across the skull (Boruah *et al.*, 2017). Thus, when BC stimulation is applied at a stiffer section, that section could move rigidly up to higher frequencies and beyond the transition frequency of surrounding sections with lower stiffness. In such a scenario, the stiffer sections could act as a large source for the wave patterns of deformations observed for the neighboring less-stiff sections such as the parietal bone, operating beyond their transition frequency.

Similarly, the higher stiffness of the bone near and around the cochlea could result in predominantly rigid body motion of the cochlea up to higher transition frequencies than the parietal plates, which in turn could reduce stimulation location dependence on the effective cochlear activation and hearing dependence in the vicinity of the cochlea. This is evidenced by clinical and experimental data showing that hearing threshold and promontory motion are comparable for stimulation at several locations on the mastoid (Dobrev *et al.*, 2016). This is also supported by finite element model predictions (Chang and Stenfelt, 2019), which have shown no influence on cochlear promontory motion between two BCHA actuators implanted in the mastoid, regardless of significant differences in their implantation position, housing geometry and interface with the mastoid's bone (BCI by Håkansson *et al.*, 2010; Bonebridge®, MED-EL, Austria).

2. Wave speed variations

The spatially varying stiffness could be affecting the spatial distribution and frequency dependence of acoustic power flow within the skull for a given stimulation location (Chang *et al.*, 2018), specifically the concentration of sound power flow in the inferior sections of the skull below 3–4 kHz. This was consistent with the observed skull surface behavior in the current study, where most of the vibrations for mastoid stimulation occurred in the inferior sections of the skull. Even for forehead stimulation, where the stimulation location was on the superior sections of the skull, a significant portion of the motion was at the inferior sections below 3 kHz. At frequencies above 6–8 kHz, all skull sections underwent deformations, as expected from the numerical predictions showing more uniform power flow distribution (Chang *et al.*, 2018).

Comparing data in Figs. 9 and 10 indicates that the variations in the spatial density of local extrema in the velocity maps appears to be related to the individual samples, rather than coupling and stimulation location. Since this corresponds to a difference in the wave propagation speeds though the skull bone, it is hypothesized to be caused by difference in the material properties, micro-structure (bone porosity) or (and) thickness of the skull plates between heads (Boruah *et al.*, 2017).

3. Skull wave patterns and hearing sensation

It should be noted that since all motion components are measured at every point, the presented measurements are sensitive to all types of modes of motion and wave propagation that involve the outer (lateral) surface of the skull bone and are sufficiently persistent during the recoding time. However, data in Figs. 5(C) and 5(D) indicate a mixture of vibration directions locally, with approximately equal response from both tangent and normal components, especially at higher frequencies ($>$2 khz), where local deformations seem to be dominant part of the motion of the skull. Even in geometrically simple shells or plates, there could be several vibration modes and corresponding modes of wave propagation (McKnight *et al.*, 2013). In addition, by accounting for the addition structural and geometrical complexity, the existence of even a greater range of propagation modes could be hypothesized. Some propagation modes, such as the in-plane compression, have estimated propagation speeds of up to 1500 m/s, which is 3–4 times faster than the wave speeds observed in the current study (350–450 m/s) based on steady state response data. However, even the slower modes of propagation observed here would reach the contralateral cochlear in the 200–500 μs range, making them relevant for the transmission of speech. In addition, there appear to be wavefronts propagating in several different directions—some circumferentially travelling to a diametrically opposing area and some traveling though the skull base,

resulting in vastly (2–5×) different trajectory lengths to reach the contralateral cochlea. This could result in interferences between wavefronts not only due to different modes of propagation, but also due to different propagation paths. Based on that, we hypothesize that in most cases the skull motion is spatially and temporally complex convolution of several modes of wave propagation. More detailed analysis of this motion could be achieved by transient excitation and recording. The exact relation between skull motion and the corresponding hearing sensation is still unclear (Kim *et al.*, 2011; Stenfelt, 2015, 2016).

V. CONCLUSIONS

The 3D LDV data acquired in this study indicate that the skull surface undergoes complex spatial motion with similar contributions from all motion components under all stimulation modes. The stimulation direction of a bone conduction hearing aid is probably of minor importance. Skull motion at low frequencies depends on site of stimulation. The source of sound propagation on the parietal plates of the skull is not the same as the location of the stimulator, suggesting different mechanical behavior of the different sections of the skull, which needs to be taken into consideration for contralateral stimulation. However, for ipsilateral stimulation, coupling at the mastoid is not sensitive to the exact coupling location, making it a more robust stimulation location for clinical audiometry and coupling of transcutaneous BCHA.

ACKNOWLEDGMENTS

Funding for this study was provided by Grant No. SNF 325230-166377 from the Swiss National Science Foundation.

Adamson, R. B. A., Bance, M., and Brown, J. A. (**2010**). "A piezoelectric bone-conduction bending hearing actuator," J. Acoust. Soc. Am. **128**(4), 2003–2008.

Borgers, C., Fierens, G., Putzeys, T., van Wieringen, A., and Verhaert, N. (**2019**). "Reducing artifacts in intracochlear pressure measurements to study sound transmission by bone conduction stimulation in humans," Otol. Neurotol. **40**(9), e858–e867.

Boruah, S., Subit, D. L., Paskoff, G. R., Shender, B. S., Crandall, J. R., and Salzar, R. S. (**2017**). "Influence of bone microstructure on the mechanical properties of skull cortical bone—A combined experimental and computational approach," J. Mech. Behav. Biomed. Mater. **65**, 688–704.

Brummund, M. K., Sgard, F., Petit, Y., and Laville, F. (**2014**). "Three-dimensional finite element modeling of the human external ear: Simulation study of the bone conduction occlusion effect," J. Acoust. Soc. Am. **135**(3), 1433–1444.

Chang, Y., Kim, N., and Stenfelt, S. (**2018**). "Simulation of the power transmission of bone-conducted sound in a finite-element model of the human head," Biomech. Model. Mech. **17**(6), 1741–1755.

Chang, Y., and Stenfelt, S. (**2019**). "Characteristics of bone-conduction devices simulated in a finite-element model of a whole human head," Trends Hear. **23**, 2331216519836053.

Chhan, D., Röösli, C., McKinnon, M. L., and Rosowski, J. J. (**2013**). "Evidence of inner ear contribution in bone conduction in chinchilla," Hear. Res. **301**, 66–71.

Dobrev, I., and Sim, J. H. (**2018**). "Magnitude and phase of three-dimensional (3D) velocity vector: Application to measurement of cochlear promontory motion during bone conduction sound transmission," Hear. Res. **364**, 96–103.

Dobrev, I., Sim, J. H., Pfiffner, F., Huber, A. M., and Röösli, C. (**2018**). "Performance evaluation of a novel piezoelectric subcutaneous bone conduction device," Hear. Res. **370**, 94–104.

Dobrev, I., Sim, J. H., Pfiffner, F., Huber, A. M., and Röösli, C. (**2019**). "Experimental investigation of promontory motion and intracranial pressure following bone conduction: Stimulation site and coupling type dependence," Hear. Res. **378**, 108–125.

Dobrev, I., Sim, J. H., Stenfelt, S., Ihrle, S., Gerig, R., Pfiffner, F., Eiber, A., Huber, A. M., and Röösli, C. (**2017**). "Sound wave propagation on the human skull surface with bone conduction stimulation," Hear. Res. **355**, 1–13.

Dobrev, I., Stenfelt, S., Röösli, C., Bolt, L., Pfiffner, F., Gerig, R., Huber, A., and Sim, J. H. (**2016**). "Influence of stimulation position on the sensitivity for bone conduction hearing aids without skin penetration," Int. J. Audiol. **55**(8), 439–446.

Dobrev, I. T. (**2014**). "Full-field vibrometry by high-speed digital holography for middle-ear mechanics," Ph.D. dissertation, Department of Mechanical Engineering, Worcester Polytechnic Institute, Worcester, MA.

Eeg-Olofsson, M., Stenfelt, S., and Granström, G. (**2011a**). "Implications for contralateral bone-conducted transmission as measured by cochlear vibrations," Otol. Neurotol. **32**(2), 192–198.

Eeg-Olofsson, M., Stenfelt, S., Håkansson, B., Taghavi, H., Reinfeldt, S., Östli, P., and Granström, G. (**2011b**). "Optimal position of a new bone conduction implant," Coch. Impl. Int. **12**, S136–S138.

Eeg-Olofsson, M., Stenfelt, S., Taghavi, H., Reinfeldt, S., Håkansson, B., Tengstrand, T., and Finizia, C. (**2013**). "Transmission of bone conducted sound–correlation between hearing perception and cochlear vibration," Hear. Res. **306**, 11–20.

Eeg-Olofsson, M., Stenfelt, S., Tjellström, A., and Granström, G. (**2008**). "Transmission of bone-conducted sound in the human skull measured by cochlear vibrations," Int. J. Audiol. **47**(12), 761–769.

Farrell, N. F., Hartl, R. M. B., Benichoux, V., Brown, A. D., Cass, S. P., and Tollin, D. J. (**2017**). "Intracochlear measurements of interaural time and level differences conveyed by bilateral bone conduction systems," Otol. Neurotol. **38**(10), 1476–1483.

Franke, E. K. (**1956**). "Response of the human skull to mechanical vibrations," J. Acoust. Soc. Am. **28**(6), 1277–1284.

Guignard, J., Stieger, C., Kompis, M., Caversaccio, M., and Arnold, A. (**2013**). "Bone conduction in Thiel-embalmed cadaver heads," Hear. Res. **306**, 115–122.

Håkansson, B., Carlsson, P., and Tjellström, A. (**1986**). "The mechanical point impedance of the human head, with and without skin penetration," J. Acoust. Soc. Am. **80**(4), 1065–1075.

Håkansson, B., Reinfeldt, S., Eeg-Olofsson, M., Östli, P., Taghavi, H., Adler, J., Gabrielsson, J., Stenfelt, S., and Granström, G. (**2010**). "A novel bone conduction implant (BCI): Engineering aspects and pre-clinical studies," Int. J. Audiol. **49**(3), 203–215.

Hartl, R. M. B., Mattingly, J. K., Greene, N. T., Jenkins, H. A., Cass, S. P., and Tollin, D. J. (**2016**). "A preliminary investigation of the air-bone gap: Changes in intracochlear sound pressure with air- and bone-conducted stimuli after cochlear implantation," Otol. Neurotol. **37**(9), 1291–1299.

Homma, K., Shimizu, Y., Kim, N., Du, Y., and Puria, S. (**2010**). "Effects of ear-canal pressurization on middle-ear bone- and air-conduction responses," Hear. Res. **263**(1), 204–215.

Hood, J. D. (**1960**). "The principles and practice of bone conduction audiometry: A review of the present position," Laryngoscope **70**(9), 1211–1228.

Hoyer, H. E., and Dorheide, J. (**1983**). "A study of human head vibrations using time-averaged holography," J. Neurosurg. **58**(5), 729–733.

Hulecki, L. R., and Small S. A. (**2011**). "Behavioral bone-conduction thresholds for infants with normal hearing," J. Am. Acad. Audiol. **22**(2), 81–92.

Hurley, R. M., and Berger, K. W. (**1970**). "Relationship between vibrator placement and bone conduction measurements with monaurally deaf subjects," J. Aud. Res. **10**(2), 147–150.

Ito, T., Röösli, C., Kim, C. J., Sim, J. H., Huber, A. M., and Probst, R. (**2011**). "Bone conduction thresholds and skull vibration measured on the teeth during stimulation at different sites on the human head," Audiol. Neurootol. **16**(1), 12–22.

Khaleghi, M., Furlong, C., Ravicz, M., Cheng, J. T., and Rosowski, J. (**2015**). "Three-dimensional vibrometry of the human eardrum with

stroboscopic lensless digital holography," J. Biomed. Opt. **20**(5), 051028-1–051028-11.
Kim, N., Homma, K., and Puria, S. (**2011**). "Inertial bone conduction: Symmetric and anti-symmetric components," J. Assoc. Res. Otolaryngol. **12**(3), 261–279.
Kompis, M., Pfiffner, F., Krebs, M., and Caversaccio, M. D. (**2011**). "Factors influencing the decision for Baha in unilateral deafness: The Bern benefit in single-sided deafness questionnaire," Adv. Otorhinolaryngol. **71**, 103–111.
Lilliefors, H. W. (**1967**). "On the Kolmogorov-Smirnov test for normality with mean and variance unknown," J. Am. Stat. Assoc. **62**(318), 399–402.
Mattingly, J. K., Greene, N. T., Jenkins, H. A., Tollin, D. J., Easter, J. R., and Cass, S. P. (**2015**). "Effects of skin thickness on cochlear input signal using transcutaneous bone conduction implants," Otol. Neurotol. **36**(8), 1403–1411.
Mattingly, J. K., Hartl, R. M. B., Jenkins, H. A., Tollin, D. J., Cass, S. P., and Greene, N. T. (**2019**). "A comparison of intracochlear pressures during ipsilateral and contralateral stimulation with a bone conduction implant," Ear Hear. **41**(2), 312–322.
McKnight, C. L., Doman, D. A., Brown, J. A., Bance, M., and Adamson, R. B. (**2013**). "Direct measurement of the wavelength of sound waves in the human skull," J. Acoust. Soc. Am. **133**(1), 136–145.
McLeod, R. W. J., Roberts, W. H., Perry, I. A., Richardson, B. E., and Culling, J. F. (**2018**). "Scanning laser Doppler vibrometry of the cranium when stimulated by a B71 bone transducer," Appl. Acoust. **142**, 53–58.
Nolan, M., and Lyon, D. J. (**1981**). "Transcranial attenuation in bone conduction audiometry," J. Laryngol. Otol. **95**(06), 597–608.
Ogura, Y., Masuda, Y., Miki, M., Takeda, T., Watanabe, S., Ogawara, T., Shibata, S., Uyemura, T., and Yamamoto, Y. (**1979**). "Vibration analysis of the human skull and auditory ossicles by holographic interferometry," in *Holography in Medicine and Biology* (Springer, Berlin), pp. 218–222.
Pfiffner, F., Caversaccio, M. D., and Kompis, M. (**2011**). "Audiological results with Baha® in conductive and mixed hearing loss," in *Implantable Bone Conduction Hearing Aids* (Karger, Basel), Vol. 71, pp. 73–83.
Reinfeldt, S., Håkansson, B., Taghavi, H., and Eeg-Olofsson, M. (**2015**). "New developments in bone-conduction hearing implants: A review," Med. Dev. (Auckland, New Zealand) **8**, 79–93.
Rodriguez, O. (**1840**). "Des lois geometriques qui regissent les desplacements d'un systeme solide dans l'espace et de la variation des coordonnees provenant de deplacements consideres independamment des causes qui peuvent les produire," J. Math. Pures Appl. **5**, 380–440.
Röösli, C., Dobrev, I., Sim, J. H., Gerig, R., Pfiffner, F., Stenfelt, S., and Huber, A. M. (**2016**). "Intracranial pressure and promontory vibration with soft tissue stimulation in cadaveric human whole heads," Otol. Neurotol. **37**(9), e384–e390.
Sim, J. H., Chatzimichalis, M., Lauxmann, M., Röösli, C., Eiber, A., and Huber, A. M. (**2010**). "Complex stapes motions in human ears," J. Assoc. Res. Otolaryngol. **11**(3), 329–341.
Sim, J. H., Dobrev, I., Gerig, R., Pfiffner, F., Stenfelt, S., Huber, A. M., and Röösli, C. (**2016**). "Interaction between osseous and non-osseous vibratory stimulation of the human cadaveric head," Hear. Res. **340**, 153–160.
Snyder, J. M. (**1973**). "Interaural attenuation characteristics in audiometry," Laryngoscope **83**(11), 1847–1855.
Sohmer, H., and Freeman, S. (**2004**). "Further evidence for a fluid pathway during bone conduction auditory stimulation," Hear. Res. **193**, 105–110.
Sohmer, H., Freeman, S., Geal-Dor, M., Adelman, C., and Savion, I. (**2000**). "Bone conduction experiments in humans—A fluid pathway from bone to ear," Hear. Res. **146**, 81–88.
Stenfelt, S. (**2006**). "Middle ear ossicles motion at hearing thresholds with air conduction and bone conduction stimulation," J. Acoust. Soc. Am. **119**(5), 2848–2858.
Stenfelt, S. (**2011**). "Acoustic and physiologic aspects of bone conduction hearing," in *Implantable Bone Conduction Hearing Aids* (Karger, Basel), Vol. 71, pp. 10–21.
Stenfelt, S. (**2012**). "Transcranial attenuation of bone-conducted sound when stimulation is at the mastoid and at the bone conduction hearing aid position," Otol. Neurotol. **33**(2), 105–114.
Stenfelt, S. (**2015**). "Inner ear contribution to bone conduction hearing in the human," Hear. Res. **329**, 41–51.
Stenfelt, S. (**2016**). "Model predictions for bone conduction perception in the human," Hear. Res. **340**, 135–143.
Stenfelt, S., and Goode, R. L. (**2005a**). "Bone-conducted sound: Physiological and clinical aspects," Otol. Neurotol. **26**(6), 1245–1261.
Stenfelt, S., and Goode, R. L. (**2005b**). "Transmission properties of bone conducted sound: Measurements in cadaver heads," J. Acoust. Soc. Am. **118**(4), 2373–2391.
Stenfelt, S., Hato, N., and Goode, R. L. (**2002**). "Factors contributing to bone conduction: The middle ear," J. Acoust. Soc. Am. **111**(2), 947–959.
Stenfelt, S., Hato, N., and Goode, R. L. (**2004**). "Fluid volume displacement at the oval and round windows with air and bone conduction stimulation," J. Acoust. Soc. Am. **115**(2), 797–812.
Stenfelt, S., Wild, T., Hato, N., and Goode, R. L. (**2003**). "Factors contributing to bone conduction: The outer ear," J. Acoust. Soc. Am. **113**(2), 902–913.
Stieger, C., Guan, X., Farahmand, R. B., Page, B. F., Merchant, J. P., Abur, D., and Nakajima, H. H. (**2018**). "Intracochlear sound pressure measurements in normal human temporal bones during bone conduction stimulation," J. Assoc. Res. Otolaryngol. **19**(5), 523–539.
Studebaker, G. A. (**1964**). "Clinical masking of air- and bone-conducted stimuli," J. Speech Hear. Disorders **29**(1), 23–35.
Stump, R., Dobrev, I., Krayenbühl, N., Probst, R., and Röösli, C. (**2018**). "In-vivo assessment of osseous versus non-osseous transmission pathways of vibratory stimuli applied to the bone and the dura in humans," Hear. Res. **370**, 40–52.
Thiel, W. (**1992**). "Die Konservierung ganzer leichen in natürlichen farben," Ann. Anat. **174**(3), 185–195.
Tonndorf, J. (**1966**). "Bone conduction. Studies in experimental animals," Acta Otolaryngol. **132**(S213), 7–9.
von Békésy, G. (**1960**). *Experiments in Hearing*, edited by Ernest Glen Wever (McGraw-Hill, New York), Vol. 8.
Watanabe, T., Bertoli, S., and Probst, R. (**2008**). "Transmission pathways of vibratory stimulation as measured by subjective thresholds and distortion-product otoacoustic emissions," Ear Hear. **29**(5), 667–673.
Yaniv, Z. (**2015**). "Which pivot calibration?," in *Medical Imaging 2015: Image-Guided Procedures, Robotic Interventions, and Modeling*, International Society for Optics and Photonics, p. 941527.
Yd, S. (**2015**). "Fast geometric fit algorithm for sphere using exact solution," arXiv:1506.02776.
Zhuang, H., Roth, Z. S., and Sudhakar, R. (**1994**). "Simultaneous robot/world and tool/flange calibration by solving homogeneous transformation equations of the form AX = YB," IEEE Trans. Robot. Autom. **10**(4), 549–554.